All-optical seeding of a light-induced phase transition with correlated disorder

Allan S. Johnson, Ernest Pastor, Sergi Batlle-Porro, Hind Benzidi,
Tetsuo Katayama, Gilberto A. de la Peña Muñoz, Viktor Krapivin,
Sunam Kim, Núria López, Mariano Trigo, Simon E. Wall

To cite this version

Allan S. Johnson, Ernest Pastor *et al*. All-optical seeding of a light-induced phase transition with correlated disorder (2024). https://hdl.handle.net/20.500.12614/3601

Licensing

Embargo

All-optical seeding of a light-induced phase transition with correlated disorder

Allan S. Johnson[1,2*+], Ernest Pastor[2,3*+], Sergi Batlle-Porro[2], Hind Benzidi[4], Tetsuo Katayama[5,6], Gilberto A. de la Peña Muñoz[7,8], Viktor Krapivin[7,8], Sunam Kim[9], Núria López[4+], Mariano Trigo[7,8], Simon E. Wall[10+].

1. IMDEA Nanoscience, Calle Faraday 9, 28049 Madrid, Spain

2. ICFO-Institut de Ciencies Fotoniques, The Barcelona Institute of Science and Technology, Av. Carl Friedrich Gauss 3, 08860 Castelldefels (Barcelona), Spain

3. CNRS, Univ Rennes, IPR (Institut de Physique de Rennes) - UMR 6251, F-35000 Rennes, France.

4. Institute of Chemical Research of Catalonia (ICIQ-CERCA), The Barcelona Institute of Science and Technology (BIST), Av. Països Catalans, 16, 43007 Tarragona, Spain

5. Japan Synchrotron Radiation Research Institute, 1-1-1 Kouto, Sayo-cho, Sayo-gun, Hyogo 679-5198, Japan.

6. RIKEN SPring-8 Center, 1-1-1 Kouto, Sayo, Hyogo 679-5148, Japan.

7. Stanford PULSE Institute, SLAC National Accelerator Laboratory, Menlo Park, CA 94025, USA.

8. Stanford Institute for Materials and Energy Sciences, SLAC National Accelerator Laboratory, Menlo Park, CA 94025, USA.

9. Pohang Accelerator Laboratory, Jigokro-127-beongil, Nam-gu, Pohang, Gyeongbuk 790-834, Republic of Korea

10. Department of Physics and Astronomy, Aarhus University, Aarhus, Denmark

**These authors contributed equally to this work.*

+Corresponding authors: allan.johnson@imdea.org, ernest.pastor@univ-rennes.fr, nlopez@iciq.es, simon.wall@phys.au.dk

Ultrafast manipulation of vibrational coherence is an emergent route to control the structure of solids. However, this strategy can only induce long-range correlations and cannot modify atomic structure locally, which is required in many technologically-relevant phase transitions. Here, we demonstrate that ultrafast lasers can generate incoherent structural fluctuations which are more efficient for material control than coherent vibrations, extending optical control to a wider range of materials. We observe that local, non-equilibrium lattice distortions generated by a weak laser pulse reduce the energy barrier to switch between insulating and metallic states in vanadium dioxide by 6%. Seeding inhomogeneous structural-fluctuations presents an alternative, more energy efficient, route for controlling materials that may be applicable to all solids, including those used in data and energy storage devices.

Solid-solid phase transitions are ubiquitous processes in nature that can be induced by changes in temperature, pressure, or applied fields, and are increasingly important for next generation, non-volatile electronics[1–6]. Thermodynamically, phase transitions are often heterogeneous, taking a percolation or nucleation-and-growth pathway[7].

However, phase transitions can also be non-thermally driven with light[8,9]. These light-induced phase transitions have the potential to transform solids in faster and more controlled ways than allowed thermodynamically.

In particular, ultrafast light-induced transitions are generally assumed to be homogenous and coherent[8,9]. The long wavelength of the light, relative to the atomic spacing, triggers coordinated and coherent motion of the atoms in many unit cells, driving a coordinated transition in a large region of the sample. The dynamics of the phase transition can be described entirely in microscopic terms and precise optical control over the transition should be possible.

Indeed, numerous experiments have shown that light can induce large scale coherent motion in solids[10–13], and recent multi-pulse experiments in quasi-1D and 2D materials have shown that the efficiency of light-induced switching can be modulated by this coherent motion[14,15], bringing the concept of coherent control from chemistry[16–18] to solids.

However, coherent control requires a well-defined long-wavelength and optically-active phonon mode that connects the crystal structures of both phases[8,14]. This excludes many technologically relevant transitions such as those in chalcogenide glasses which exploit the crystalline-to-amorphous transitions for data storage[2,3,5]. It is thus unclear if ultrafast processes will bring any benefit for controlling phase transitions in these materials.

Here we demonstrate an alternative, incoherent, route for material control on the ultrafast timescale. We improve the energy efficiency of the insulator-metal phase transition in VO_2 by up to 6% when compared to a single pulse excitation by exciting the sample with two pulses. The first pulse generates both large-scale coherent structural motion and also temporally incoherent, yet spatially correlated, localized lattice displacements. However, we find that the incoherent local modes, rather than the coherent motion, are responsible for lowering the energy barrier for the formation of the metallic phase. Density functional theory suggests that interactions between polarons are responsible for the transient barrier reduction. As this correlated disorder can, in principle, be induced in any solid, the incoherent approach may expand the applicability of ultrafast control to a broad range of materials that cannot be coherently steered.

VO_2 is a prototypical system for understanding phase transitions in quantum materials[19]. At high temperatures the system is in a metallic rutile phase (R), but below T_c ~ 60 ºC the vanadium ions pair and twist around the rutile c-axis resulting in a monoclinic insulating phase (M1). Weak photoexcitation of the M1 phase generates coherent phonons, which dynamically modulate the amplitude of the dimerization and tilting of the vanadium atoms[13,20].

Excitation of the M1 phase above a critical fluence threshold F_{th} drives the system to the metallic rutile phase, R. Initially it was assumed that the coherent motion observed at low fluences continues through the phase transition[21,22], but more recent work showed that the coherent motion is quickly transformed into a broad range of incoherent phonon modes and the transition is driven by disorder[23,24]. This places VO_2 between charge density wave systems, which are transformed by a few long-wavelength modes[25,26], and crystalline-amorphous phase transitions in which local uncorrelated distortions drive the transition[3,4,27]. Thus, VO_2 is an ideal material in which to test how ultrafast control can be applied in systems showing both coherence and disorder.

Ultrafast control of a phase transition

We explore optical control of the phase transition by performing multi-pulse excitation experiments in a high-quality single crystalline sample of VO_2. We first use a weak pulse (henceforth labelled *prep* pulse) to *prepare* a non-thermal coherently vibrating state in the M1 phase. Subsequently we use a second pulse (labelled *push*) to further excite the sample after a certain delay, t_{pp}, and detect if the phase transition occurred with a third *probe* pulse after a time t_d (**Fig 1a**).

Fig 1b shows the transient reflectivity as a function of probe delay for a fixed *prep-push* delay, t_{pp} = -700 fs, corresponding to 4 periods of the coherent 5.7 THz mode in VO_2. The figure displays the cases where the *push* pulse has both sufficient and insufficient fluence to initiate the phase transition. As the excitation is in-phase, a weak *push* pulse amplifies the coherent motion as we remain in the M1 phase. However, a strong *push* pulse induces a larger change in reflectivity and the coherent phonon is suppressed, indicating a transformation to the R phase.

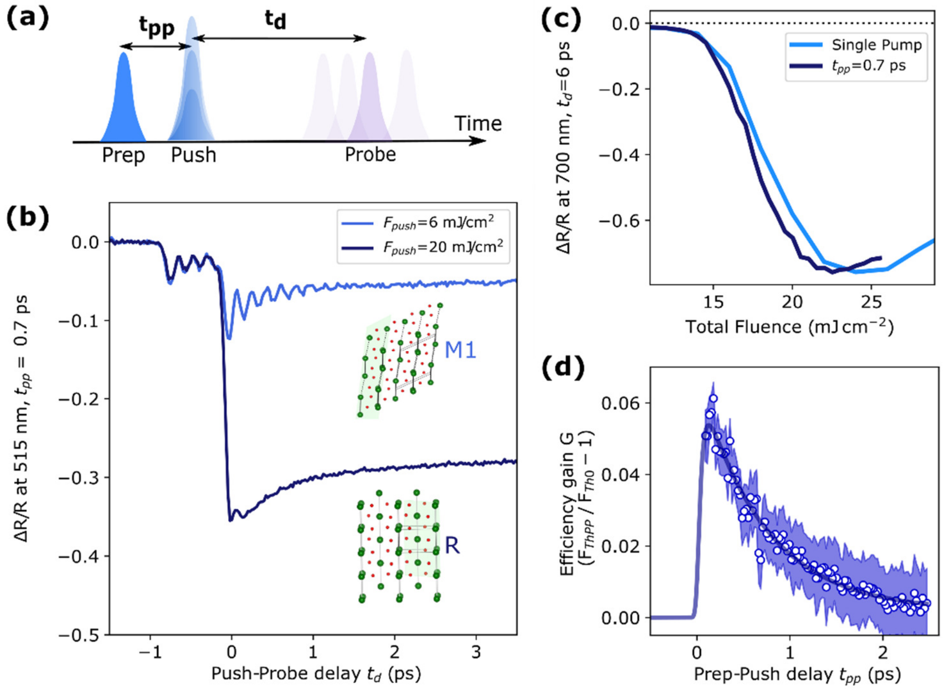

Fig 1: (a) Double pump experimental scheme. (b) Transient reflectivity signals as a function of t_d. A low fluence *prep* pulse (F_{prep} =5 mJ/cm²) generates coherent phonon oscillations in the M1-phase, while a second excitation can amplify the coherent motion (6 mJ/cm²) or drive the system into the R phase (20 mJ/cm²). (c) Total fluence dependence of the transient reflectivity for a single pulse and double-excitation measured at t_d=6 ps (with F_{prep} =5.5 mJ/cm²). (d) Relative gain, *G*, in the fluence threshold for a prep-push experiment in comparison to a single pulse experiment, as a function of prep-push delay. The standard error on the efficiency is shown by the shaded region. There is notable gain at small time delays below the single-

pulse fluence requirement. The solid line shows a double exponential fit with 40±8 fs rise and 650±49 fs fall time, convolved with the 50-fs experimental resolution. For experimental and fitting details see methods.

Fig 1c shows how the transient reflectivity changes as a function of the total incident fluence (F_{prep}+ F_{push}). For a single pulse excitation, a sudden change in slope at around 15 mJ/cm^2 is observed. This transition from relatively small changes in reflectivity with fluence to a much higher rate of change marks the fluence threshold, F_{TH0}, at which the system begins to transform to the metallic phase. Above this fluence, the signal grows rapidly before saturating. Remarkably, for a double-pulse scheme we find that the total energy needed to both initiate and saturate the transition is reduced compared to the single pulse, thus indicating that multiple excitations can lower the energy needed to drive the phase transformation in VO_2. We note, the use of a threshold fluence is a different criterion to other works, which instead focused on changes in volume fraction converted[14,15], rather than the energy required to initiate the transition as used in this work.

Next, we explore the dynamics of the threshold reduction. We fix F_{prep} to 5.5 mJ/cm^2, to ensure that a coherent vibrational state is induced, and scan the push fluence, F_{push}, for different prep-push delays in order to determine $F_{THPP}(t_{pp})$. F_{TH0} can be mathematically extracted using a variety of fitting procedures which we find give consistent results, see SI. In **Fig 1d** we plot the relative efficiency gain, $G=F_{THPP}(t_{pp})/F_{TH0}-1$, as a function of *prep-push* delay, where 0 corresponds to no gain. If coherent motion modulated the threshold energy, we would expect this quantity to oscillate with the phonon period, whereas, if the transition is only limited by the total energy supplied, and not how it is supplied, G should be independent of time.

We observe neither of these scenarios. Instead, the threshold is strongly reduced at short delays and recovers with an approximately 650 fs time constant before returning to zero after 2 ps, indicating that the threshold energy can be reduced through an incoherent but nonthermal pathway. Although we cannot measure close to time zero due to coherent interference between the *prep* and *push* fields, G must return to zero at t_{pp} = 0 to recover the single pulse threshold. Therefore, the gain must rapidly rise within ~125 fs to approximately 6%. We fit this data with a double exponentially with a 40±8 fs rise time and a 650±49 fs fall time (see **methods**).

Structural dynamics of the photoexcited M1 phase

Photoinduced changes in the absorption following the initial photoexcitation cannot account for the change in switching efficiency as they are both too small and should display the coherent response in the threshold change (see **SI: Prep-induced change in absorption**) and previous photoemission experiments did not see dynamics on the timescale seen here[28]. Therefore, we examine if incoherent structural effects could be responsible for the energy saving. **Fig 2a** shows total X-ray scattering measurements, collected at the SACLA XFEL around the (-122) and (-113) M1 Bragg peaks. The M1 peaks measure the long-range order of the vanadium dimers, while the diffuse scattering around the peaks measures momentum dependence of local fluctuations in the structure.

Fig 2b shows the long-range structural dynamics after we excite the system with 9 mJ/cm^2, just below the fluence required to initiate the phase transition (**SI: Bragg Peak Fluence Dependence)**. The intensity of the Bragg peaks drops rapidly within 65 fs, around our temporal resolution, before partially recovering over a few hundred femtoseconds. On top of these dynamics, the large-amplitude coherent vanadium motion can be observed. The signal decrease can then be ascribed to a combination of coherent displacements and a Debye-Waller-like suppression resulting from incoherent motion[23].

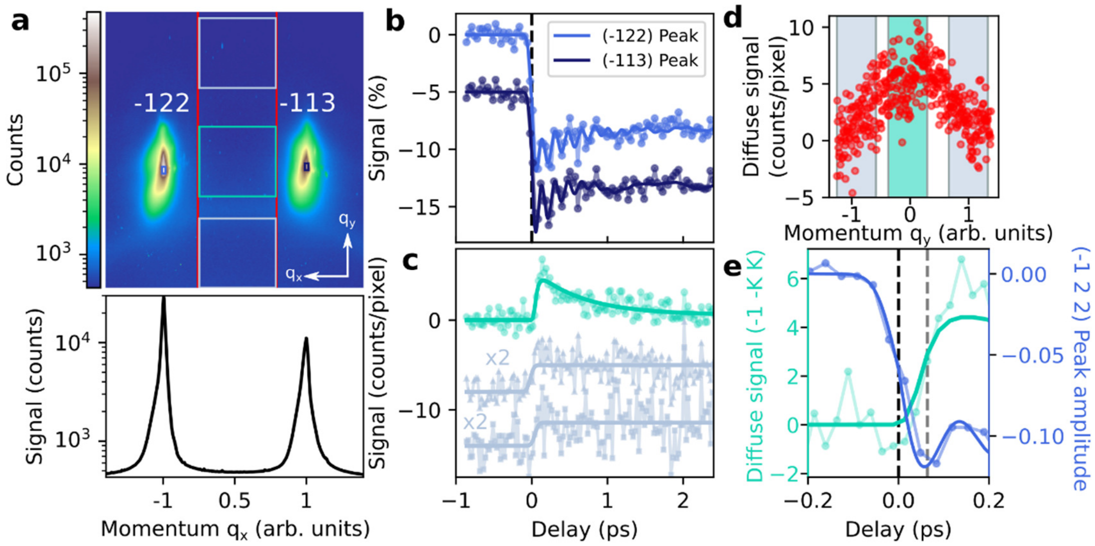

Fig 2: (a) Image of 12 keV X-ray scatter from single crystal VO_2. Bragg peaks are labeled by the corresponding Miller indices of the M1 phase, while solid boxes correspond to regions of interest (ROIs). Also shown is the signal integrated across the vertical q_y direction. (b) Dynamics near the (-122) and (-113) Bragg peaks below threshold (small blue ROIs, panel a), showing a rapid decrease in amplitude after photoexcitation and strong coherent phonon oscillations. (c) Temporal dynamics of diffuse scatter along the q_x=(-1 -K K) direction between the Bragg peaks (green ROI in panel a). Also shown are two regions of interest (light-blue ROIs in panel a) which show only a step-function behavior. (d) Diffuse scatter averaged across the q_x direction at 150 fs delay (red ROI panel a), with the ROIs of the different diffuse ROIs highlighted, showing the transient diffuse scattering is centered between the two peaks at $q_y=0$. (e) Dynamics around time zero for both the normalized Bragg traces and the mean of the diffuse scatter. Dashed lines indicate the half-fall and half-rise times of the two signals, respectively. Solid lines in plots b, c and e are from fits, see methods.

Fig 2c analyses the diffuse scattering due to incoherent phonons. We find that the diffuse signal is primarily confined to a stripe of reciprocal space along the (-1 -K K) monoclinic direction spanning wavevectors from (-122) to (-113) (**Fig 2d** and red box in **Fig 2a**). The signal shows a rapid increase upon photoexcitation, followed by a recovery within 2 picoseconds. The dynamics are independent of wavevector along the (-1 -K K) direction within our signal to noise. Outside this stripe-region we observe lower signal levels and a step-like behaviour as shown by the two light-blue ROIs (**Fig 2a**) and traces (**Fig 2c**).

The dynamics of the diffuse stripe-region upon weak excitation show a remarkable similarity to the gain dynamics shown in **Fig 1c** in which the system is re-excited after an initial weak excitation. Critically, the increase in the diffuse scattering is delayed by ~50fs relative to the drop in M1 Bragg peak intensity (**Fig 2e**) and we can fit the diffuse dynamics with the same function as the double-pulse gain dynamics in **Fig 1c (See methods).**

Electronic and atomic structure simulations

Stripe-shaped fluctuations in diffuse scattering result from correlated disorder, where the motion remains correlated in one dimension, but is disordered in the others[29]. In our case the stripes correspond to correlated fluctuations along the body diagonal of the rutile unit cell ($[111]_R$ - rutile notation). This suggests that correlated fluctuations along the $[111]_R$ are responsible for the energy saving in the multi-excitation scheme that exhibit the same time dependence (**Fig 1c**). We note that the $[001]_R$ direction is often considered important for the physics of VO_2, but correlations along this direction produce a very different scattering pattern, as demonstrated in **Supplementary Figure S3.**

To understand the origins of the correlated fluctuations, we turn to Density Functional Theory (DFT, **see methods for details**). Within the M1 phase, we find both the ground state (**Fig 3a**) and a meta-stable structurally distorted polaronic state (**Fig 3b**). The polaronic state is primarily electronically confined to two adjacent V sites along monoclinic a-axis (rutile c-axis) with an estimated electronic radius of 3.1 Å, causing a change in V-V bonds (**see SI: DFT Structural Results**). Notably, the polaron exhibits a charge disproportionation where the initial two-V^{4+} charges are separated into one V^{3+} and one $V^{5+,}$ stabilized by a second-order Jahn-Teller (SOJT) octahedral distortion that extends beyond the two electronically effected ions.

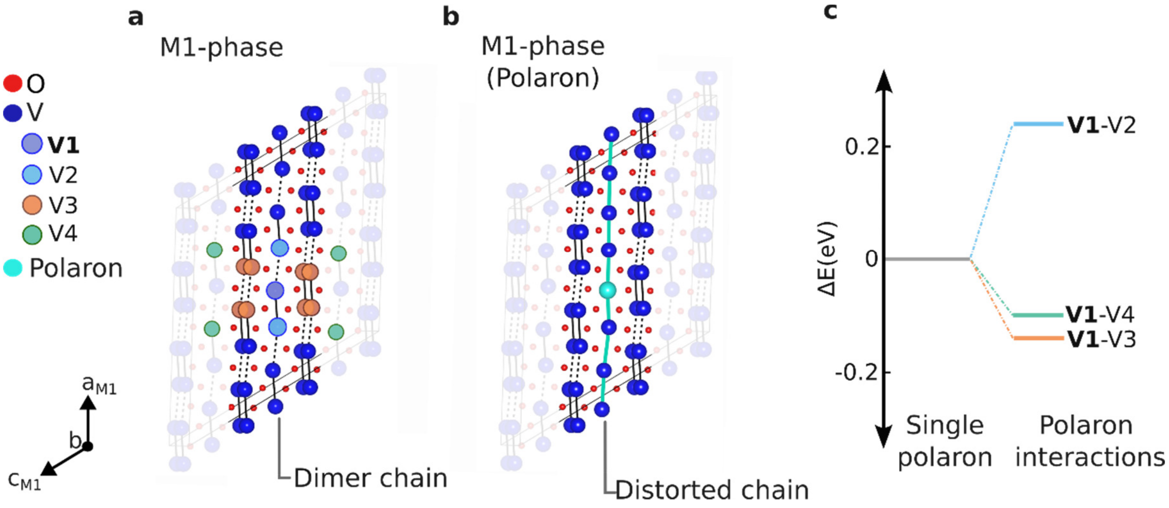

Fig 3: (a) Crystal structure of the undistorted M1 phase calculated via DFT and symmetry-equivalent vanadium sites indicated (see methods). (b) Polaron-distorted M1 structure with location of the polaronic distortion. Also highlighted are the relaxed dimer chains resulting from the polaron distortion. (c) Energetics of the polaron-polaron interactions (obtained in a 2x2x2 supercell) for different geometric configurations corresponding to the labelled vanadium atoms in a (see methods). When polarons are at neighboring sites along the monoclinic a-axis (rutile c), there is a high energy penalty (V1-V2). However, if the polarons are on neighboring chains (V1-V3, V1-V4) then the energy cost is reduced.

Such polarons could be expected to form following photoexcitation[30,31], but a local defect alone cannot explain the stripe-shaped diffuse features we measure as these emerge due to correlated fluctuations[29]. Therefore, we examine possible polaronic interactions. For clarity hereafter, we consider the polaron to be located at the V^{3+} site.

We find that the energy of the two polaron system strongly depends on the relative location of the distortions (**Fig 3c**). In particular, two polarons at neighboring lattice sites along the monoclinic a-axis (i.e. in the same dimer chain) induce a large energy penalty, whereas two neighboring polarons along the rutile body diagonal (i.e; in neighbouring dimer chains) reduce the energy penalty. This favorable interaction direction, captured by DFT, corresponds to the direction associated with the diffuse stripe features observed **Fig 2**. Based on these observations we propose that cooperative distortions between polarons along $[111]_R$ are responsible for reducing the barrier to the metallic phase.

The Mechanism of Control

Fig 4 summarizes our observations about the control of the phase transition and dynamic modulation of the energy barrier (**Fig 4a**). Photoexcitation first induces coherent motion that is correlated in all three dimensions; this reduces the Bragg intensity of the M1 peaks, without increasing the diffuse scattering, but has no appreciable effect on the threshold energy (**Fig 4b**). Next, after ~50 fs, this fully correlated motion is reduced and only correlations along $[111]_R$ persist giving rise to stripes in the diffuse scatter and which we associate to cooperative polarons (**Fig 4c**).

Once formed, the polaronic state lowers the barrier to the metallic R phase. Consequently, driving the phase transition by exciting this state can be achieved with less energy in agreement with our double-pulse gain data. Subsequently, after a few picoseconds, the cooperative polaron interactions are lost and the system recovers a thermal state, which manifests in a more homogenous thermal diffuse pattern. Re-excitation of this state with the *push* beam does not cause any modulation of the transformation barrier (**Fig 4d**).

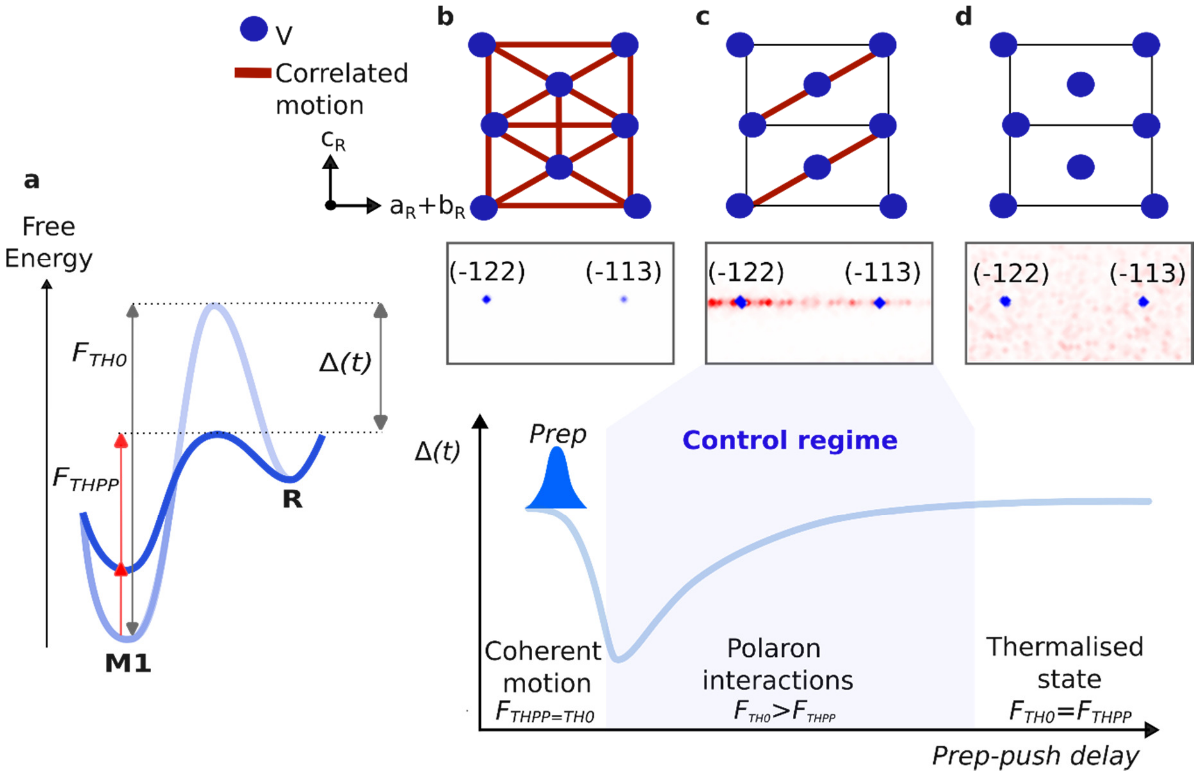

Fig 4 a Schematic energy for the M1 and R phase and effect of a multi-pulse excitation. The phase transition from M1 to R is separated by an energy barrier which can be overcome with a single laser pulse that excites the system above a certain fluence threshold (F_{THO}). Pre-excitation of the M1 phase with a weak (prep) pulse increases the temperature (free energy), but also creates structural fluctuations which enable a transient change in the energy barrier (Δ(t)) and a reduction of the transition threshold (F_{THPP}) in a multi-pulse excitation regime. **b-d** Representation of the atoms intersecting the $[111]_R$ (rutile notation) direction (top) alongside modelled diffuse intensity maps (middle) and the time evolution of the energy barrier (bottom). **b** Initially the phonon displacement is coherent and correlated in three dimensions resulting in a reduction of the M1 Bragg peak intensities without a rise in the diffuse scattering. Coherent motion has no appreciable effect in the energy barrier. **c** After 50 fs the coherence is lost and correlations remain only along the $[111]_R$ direction due to polaronic interactions. This results in the emergence of a stripe-shaped diffuse scatter and a reduction of the energy barrier when the system is re-excited in the strong correlation regime. **d** Finally, the correlations along the $[111]_R$ direction decay as the system thermalizes and the single-pulse energy barrier is recovered.

Recently, theoretical models have suggested that the energy barrier between the insulating and metallic phase in VO_2 is reduced if the vanadium ions first untwist before losing the dimerization along the rutile c-axis, rather than moving in a direct and synchronized fashion to the high symmetry state[32]. Our experimental results validate this principle. However, our data reveal that the energy saving results from correlated motion between vanadium ions on *different* c-axis chains.

Furthermore, the $[111]_R$ direction is also different from that of the k-vector associated with the phase transition, $[101]_R$, but is consistent with the dominant diffuse scattering observed in metallic phase[33]. This suggests that, for driving the phase transition, it is more important to produce correlated rutile-like distortions along the $[111]_R$ rather than a specific long-wavelength distortions at the $[101]_R$ phase transition wavevector.

While DFT is unable to estimate the lifetime of the polaron state, it seems highly likely that the coherent distortion first breaks down into polarons that are correlated along $[111]_R$ before being converted to random thermal motion. As polaron formation takes ~50 fs (**Fig 2e**), these distortions do not contribute to the phase transition pathway when the system is excited with a single sub-50-fs pulse femtosecond pulse. However, we expect that the phase transition threshold is reduced for longer single pulses as the falling edge of the laser beam could excite polarons created by the leading edge.

Future Perspectives

One interesting consequence of the inhomogeneous seeding is that, as the distortion acts to lower the energy barrier between the two phases (**Fig. 4a**), the excess energy needed to drive the transition in the double pump scheme is lower than for a single pump. This excess energy is ultimately converted to heat and thus the resulting metallic phase will be at a correspondingly lower temperature. The dynamic lowering of the barrier also means we are able to selectively reduce the energy required for the light-induced phase transition without also increasing the probability of thermal switching, in contrast to other methods for improving the efficiency of switching processes.

Optimization of the energy savings beyond the 6% we report may be possible via targeted optimization of how the correlated disorder is generated and harnessed. This might be achieved by more selective excitation of the relevant polaron modes, by tuning the *prep* pulse wavelength or fluence, or by using more complex sequences of preparation pulses, but further investigation along these lines is needed.

Notably, contrary to structural coherence, correlated disorder can, in principle, be induced in any solid. Consequently, the inhomogeneous seeding strategy we report, might be applicable to a broad range of solids, including those used in energy and data strange applications, for which there is no available optical coherent control route that enables rapid phase changes while still maintaining high energy and thermal efficiency.

References

1. Simpson, R. E. *et al.* Interfacial phase-change memory. *Nature Nanotech* **6**, 501–505 (2011).
2. Teo, T. Y. *et al.* Programmable chalcogenide-based all-optical deep neural networks. *Nanophotonics* **11**, 4073–4088 (2022).
3. Loke, D. *et al.* Breaking the Speed Limits of Phase-Change Memory. *Science* **336**, 1566–1569 (2012).

4. Simpson, R. E. *et al.* Toward the Ultimate Limit of Phase Change in $Ge_2Sb_2Te_5$. *Nano Lett.* **10**, 414–419 (2010).
5. Matsunaga, T. *et al.* From local structure to nanosecond recrystallization dynamics in AgInSbTe phase-change materials. *Nature Mater* **10**, 129–134 (2011).
6. Samizadeh Nikoo, M. *et al.* Electrical control of glass-like dynamics in vanadium dioxide for data storage and processing. *Nat Electron* **5**, 596–603 (2022).
7. Binder, K. & Binder, K. Theory of first-order phase transitions. *Reports on Progress in Physics* **50**, 783–859 (2016).
8. de la Torre, A. *et al. Colloquium:* Nonthermal pathways to ultrafast control in quantum materials. *Rev. Mod. Phys.* **93**, 041002 (2021).
9. Giannetti, C. *et al.* Ultrafast optical spectroscopy of strongly correlated materials and high-temperature superconductors: a non-equilibrium approach. *Advances in Physics* **65**, 58–238 (2016).
10. Sokolowski-Tinten, K. *et al.* Femtosecond X-ray measurement of coherent lattice vibrations near the Lindemann stability limit. *Nature* **422**, 287–289 (2003).
11. Beaud, P. *et al.* A time-dependent order parameter for ultrafast photoinduced phase transitions. *Nature Materials* **13**, 923–927 (2014).
12. Hase, M. *et al.* Optical control of coherent optical phonons in bismuth films. *Applied Physics Letters* **69**, 2474–2476 (1996).
13. Wall, S. *et al.* Ultrafast changes in lattice symmetry probed by coherent phonons. *Nature Communications* **3**, 721 (2012).
14. Horstmann, J. G. *et al.* Coherent control of a surface structural phase transition. *Nature* **583**, 232–236 (2020).
15. Maklar, J. *et al.* Coherent light control of a metastable hidden state. *Sci. Adv.* **9**, eadi4661 (2023).
16. Hildner, R., Brinks, D. & Van Hulst, N. F. Femtosecond coherence and quantum control of single molecules at room temperature. *Nature Phys* **7**, 172–177 (2011).
17. Dantus, M. Coherent Nonlinear Spectroscopy : From Femtosecond Dynamics to Control. *Annu. Rev. Phys. Chem.* **52**, 639–679 (2001).
18. Warren, W. S., Rabitz, H. & Dahleh, M. Coherent control of quantum dynamics: The dream is alive. *Science* **259**, 1581–1589 (1993).
19. Shao, Z., Cao, X., Luo, H. & Jin, P. Recent progress in the phase-transition mechanism and modulation of vanadium dioxide materials. *NPG Asia Materials* **10**, 581–605 (2018).
20. Wall, S. *et al.* Tracking the evolution of electronic and structural properties of VO_2 during the ultrafast photoinduced insulator-metal transition. *Physical Review B* **87**, 115126 (2013).
21. Baum, P., Yang, D. S. & Zewail, A. H. 4D visualization of transitional structures in phase transformations by electron diffraction. *Science* **318**, 788–792 (2007).
22. Cavalleri, A., Dekorsy, T., Chong, H. H. W., Kieffer, J. C. & Schoenlein, R. W. Evidence for a structurally-driven insulator-to-metal transition in VO_2: A view from the ultrafast timescale. *Physical Review B* **70**, 161102(R) (2004).
23. Wall, S. *et al.* Ultrafast disordering of vanadium dimers in photoexcited VO_2. *Science* **362**, 572–576 (2018).
24. De La Peña Muñoz, G. A. *et al.* Ultrafast lattice disordering can be accelerated by electronic collisional forces. *Nat. Phys.* (2023) doi:10.1038/s41567-023-02118-z.
25. Demsar, J., Biljaković, K. & Mihailovic, D. Single particle and collective excitations in the one-dimensional charge density wave solid $K_{0.3}MoO_3$ probed in real time by femtosecond spectroscopy. *Physical Review Letters* **83**, 800–803 (1999).
26. Huber, T. *et al.* Coherent structural dynamics of a prototypical charge-density-wave-to-metal transition. *Physical Review Letters* **113**, 026401 (2014).
27. Waldecker, L. *et al.* Time-domain separation of optical properties from structural transitions in resonantly bonded materials. *Nature Mater* **14**, 991–995 (2015).
28. Wegkamp, D. *et al.* Instantaneous band gap collapse in photoexcited monoclinic VO_2 due to photocarrier doping. *Physical Review Letters* **113**, 216401 (2014).

29. Keen, D. A. & Goodwin, A. L. The crystallography of correlated disorder. *Nature* **521**, 303–309 (2015).
30. Brazovskii, S. Self-localized excitations in the Peierls-Frahlich state. *Sov. Phys. JETP* **51**, 342–353 (1980).
31. Pastor, E. *et al.* In situ observation of picosecond polaron self-localisation in α-Fe_2O_3 photoelectrochemical cells. *Nature Communications* **10**, 3962 (2019).
32. Grandi, F., Amaricci, A. & Fabrizio, M. Unraveling the Mott-Peierls intrigue in vanadium dioxide. *Phys. Rev. Research* **2**, 013298 (2020).
33. Budai, J. D. *et al.* Metallization of vanadium dioxide driven by large phonon entropy. *Nature* **515**, 535–539 (2014).
34. Henke, B. L., Gullikson, E. M. & Davis, J. C. X-Ray Interactions: Photoabsorption, Scattering, Transmission, and Reflection at E = 50-30,000 eV, Z = 1-92. *Atomic Data and Nuclear Data Tables* **54**, 181–342 (1993).
35. Vidas, L. *et al.* Does VO^2 Host a Transient Monoclinic Metallic Phase? *Physical Review X* **10**, 031047 (2020).
36. Kresse, G. & Hafner, J. *Ab initio* molecular dynamics for liquid metals. *Phys. Rev. B* **47**, 558–561 (1993).
37. Perdew, J. P., Burke, K. & Ernzerhof, M. Generalized Gradient Approximation Made Simple. *Phys. Rev. Lett.* **78**, 1396–1396 (1997).
38. Dudarev, S. L., Botton, G. A., Savrasov, S. Y., Humphreys, C. J. & Sutton, A. P. Electron-energy-loss spectra and the structural stability of nickel oxide: An LSDA+U study. *Phys. Rev. B* **57**, 1505–1509 (1998).
39. Sun, J., Ruzsinszky, A. & Perdew, J. P. Strongly Constrained and Appropriately Normed Semilocal Density Functional. *Phys. Rev. Lett.* **115**, 036402 (2015).

Methods

Optical Prep-Push Experiments

A Ti:Sapphire Legend Elite Duo laser supplied by Coherent produces pulses of 35 fs duration at a central wavelength of 800 nm and with an energy of 1 mJ at a 5 kHz repetition rate. The beam is first split into pump and probe pulses, and then the pump into *prep* and *push* using a Michelson interferometer where the power of both arms is controlled independently and a motorized delay stage controls the *prep-push* delay. After this, both *prep* and *push* pass through a chopper and to another delay stage that controls the *push-probe* delay. The *prep* and *push* beams are focused to a spot size 10x bigger than the probe, incident on the sample at an angle of 45 deg. The fluence is calculated using a beam-size extracted by fitting a Gaussian profile to an image recorded by a CMOS camera. The visible probe supercontinuum probe is generated by focusing the 800nm pulses into a sapphire crystal, and subsequently compressed with a pair of chirped mirrors. The reflection of the probe beam from the sample is collected and passed to a spectrometer.

Total X-ray Scattering Experiments

X-ray scattering experiments were performed at the SACLA X-ray free electron laser in Japan. A multi-millimeter sized single crystal of VO_2 with sample normal along the $[1\ 1\ 0]_R$ (rutile) direction was illuminated by 12 keV X-rays at a grazing incidence of ≈0.3°, which probes a depth of approximately 100 nm[34]. Negligible diffuse scattering at negative time delays and resolution limited Bragg peak widths suggest the crystal is of exceptionally high quality. The resulting scattered X-rays were captured by a multiport charge-coupled device detector placed 106 mm downstream. The VO_2 was then photoexcited with optical pump pulses at a central wavelength of 800 nm and 40 fs pulse duration incident at an angle of 5° relative to the X-ray probe, giving an optical penetration depth of around 60 nm[35]. The timing jitter between optical and x-ray pulses was measured and corrected using a spatially-encoded timing tool, resulting in a temporal resolution of 50 fs. Fluence scans were performed to determine the point at which the phase transition was initiated through a bi-linear fit to the drop in Bragg-peak signal level, and subsequent measurements were performed below this fluence (See SI). In these scans we found that we were able to suppress the Bragg peak by ~70% suggesting that the probe depth was comparable to the pumped depth.

Time-Trace Fitting

We fit both the efficiency gain $G(t_{pp})$ in double pump experiments and the time dependence of the correlated diffuse scatter along the (-1 –K K) direction by using a double exponential function $S(t) = H(t) * \left[1 - e^{-t/\tau_1}\right]\left[Ae^{-t/\tau_2} + B\right]$, where H is the Heaviside function, τ_1 describes the rise time of the signal while τ_2 describes the decay, A is the amplitude of the transient and B describes the long-term asymptotic change in signal level. The trace was then convolved with a Gaussian of FWHM 50 fs to represent our temporal resolution. We find both the efficiency gain and diffuse signal are well described when τ_1 = 40±8 fs and τ_2 = 650±49 fs, as shown in Figures 1d and 2c of the main text, which were chosen by initially allowing free-fitting of the optical data. Free fitting of the diffuse scatter returns unphysically fast rise times (<10 fs) and depends sensitively on the ROI used; fixing these two parameters, however, leads to a robust fitting and good agreement. A double exponential format was chosen to best describe the incoherent formation and decay of the structural defects. The dynamics of the Bragg peaks were fit using

$$S(t) = A * \left[\mathrm{erf}\left(\frac{t}{\tau_1}\right) + 0.5\right]\left[Be^{-t/\tau_2} + Ce^{-t/\tau_a}\cos\omega_a t + De^{-t/\tau_b}\cos\omega_b t + E\right].$$

It was necessary to introduce a 15 fs offset in time between the dynamics of the Bragg peaks and that of the diffuse scatter in order to obtain good fitting of the rising edge; this could be due to the need for the long term structural motion to breakdown before the polarons can form, or simply due to the different forms of fitting functions used. This does not, however, affect any of the analysis or conclusions presented here.

Diffuse scattering simulations

The reciprocal space maps shown in Fig 4b-d were calculated by performing the Fourier transform of the positions of 20x20x20 vanadium ions. First the diffuse scattering pattern was calculated for the perfect monoclinic structure, which acts as a reference. Then the vanadium ions were moved in three different ways. The coherent simulation moved each V ion by the same distance in a manner that preserves the M1 symmetry. The correlated case moved all ions on the same $[111]_R$ chain by the same displacement, but the displacements were random between chains. The thermal case moved each vanadium ion in a random and independent way. The resulting diffuse patterns were then subtracted from the reference signal.

Computational methods

Density-functional theory (DFT) calculations were carried out using the Vienna ab initio simulation package (VASP)[36] and the projector augmented wave (PAW) method[37]. The PBE and HSE functionals were used to model exchange and correlation effects, with HSE06 being the conventional mixing and screening (α = 0.25 and ω = 0.2 Å^{-1})

approach. The DFT+U method[38] was used with a U-parameter applied to the V-3d orbitals; We used $U_{eff} = U - J = 3$ eV with a J value of 1.0 eV. Supercells with (3×3×3) (324 atoms) were used for most calculations, with (6×6×6) and (4×4×4) Monkhorst–Pack grids for PBE, PBE+U and HSE, respectively. K-point meshes were adjusted for larger supercells. A plane wave cut-off energy of 500 eV was used, and the calculations were converged to energies within 10^{-7} eV for electronic structure and ionic relaxations to forces within 10^{-4} eV Å^{-1}. In our work, we localized electrons at specific sites in VO_2 by distorting VO_6 octahedra in the undistorted structure. To explore the stability of the distorted structure, we utilized a combination of GGA+U and the SCAN density functional[39]. We controlled the number of valence electrons and checked the charge density, local lattice environment, and magnetic moment to ensure accurate occupation. We also used chrome pseudopotentials to create wavefunctions with localized electrons. This method is a very efficient approach to form stable polarons. To calculate the polaron formation energy, one needs to compare the total energies of two different electronic states: the delocalized state and the localized state. The delocalized state is typically a band-like state, while the localized state is polaronic. The polaron formation energy (E_{pol}^{DFT}) can be defined as the energy difference between the total energy of the delocalized state (E_{loc}^{undist}) and the total energy of the localized state (E_{loc}^{dis}). Thus, $E_{pol}^{DFT} = E_{loc}^{dis} - E_{deloc}^{undist}$. Determination of the polaron radius by fitting a three-dimensional Gaussian to the electron density to determine the radius where the density decreases to a desired percentage value (see Figure S4). The properties of the polaron like its extension were benchmarked in a large supercell of 3x3x3. However, to calculate the polaron-polaron interactions, a unit cell size of 2x2x2 was used as at least 10 configurations were explored individually. The symmetrical equivalence of different sites (as labelled in Fig3.a) was determined from the M1 unit cell in this reduced cell.

Data availability

Source data are available with this paper. Other data that support the findings of this study are available from the corresponding authors upon reasonable request. The DFT computed structures can be found in the ioChem-BD repository:

https://iochem-bd.iciq.es/browse/review-collection/100/64614/b0bbca34e491db60d6fe07b3

Author contributions

S. E. W. and M. T. conceived of the project. S. B. P. and E. P. performed the optical measurements and analyzed the data together with A. S. J and S. E. W.

A. S. J., E. P., T. K., G. A. d. l. P. M., V. K., S. K., M.T. and S. E. W. performed diffuse scattering measurements. A. S. J. and G. A. d. l. P. M. analyzed the X-ray data.

H. B. and N. L performed the polaron calculations.

A. S. J., E. P. and S. E. W. wrote the paper with input from all authors.

Competing Interests

The authors declare no competing interests.

Acknowledgements

X-ray measurements were performed at BL3 of SACLA with the approval of the Japan Synchrotron Radiation Research Institute (JASRI) (proposal nos. 2018A8007, 2019A8038 and 2019B8075).

ASJ acknowledges support from: ERC AdG NOQIA; MICIN/AEI (PGC2018-0910.13039/501100011033, CEX2019-000910-S/10.13039/501100011033, Plan National FIDEUA PID2019-106901GB-I00, FPI; MICIIN with funding from European Union NextGenerationEU (PRTR-C17.I1): QUANTERA MAQS PCI2019-111828-2); MCIN/AEI/ 10.13039/501100011033 and by the “European Union NextGeneration EU/PRTR" QUANTERA DYNAMITE PCI2022-132919 within the QuantERA II Programme that has received funding from the European Union’s Horizon 2020 research and innovation programme under Grant Agreement No 101017733Proyectos de I+D+I “Retos Colaboración” QUSPIN RTC2019-007196-7); Fundació Cellex; Fundació Mir-Puig; Generalitat de Catalunya (European Social Fund FEDER and CERCA program, AGAUR Grant No. 2021 SGR 01452, QuantumCAT \ U16-011424, co-funded by ERDF Operational Program of Catalonia 2014-2020); Barcelona Supercomputing Center MareNostrum (FI-2023-1-0013); EU (PASQuanS2.1, 101113690); EU Horizon 2020 FET-OPEN OPTOlogic (Grant No 899794); EU Horizon Europe Program (Grant Agreement 101080086 — NeQST), National Science Centre, Poland (Symfonia Grant No. 2016/20/W/ST4/00314); ICFO Internal “QuantumGaudi” project; European Union’s Horizon 2020 research and innovation program under the Marie-Skłodowska-Curie grant agreement No 101029393 (STREDCH) and No 847648 (“La Caixa” Junior Leaders fellowships ID100010434: LCF/BQ/PI19/11690013, LCF/BQ/PI20/11760031, LCF/BQ/PR20/11770012, LCF/BQ/PR21/11840013).

This project has received funding from the “Presidencia de la Agencia Estatal de Investigación” within the PRE2020-094404 predoctoral fellowship, the Spanish Ministry of Science and Innovation (Ref. No. PID2021-122516OB-I00, Severo Ochoa Center of Excellence CEX2019-000925-S 10.13039/501100011033).

T.K. acknowledges support from JSPS KAKENHI (grant nos. JP19H05782, JP21H04974 and JP21K18944).

E.P acknowledges the support form IJC2018-037384-I funded by MCIN/AEI /10.13039/501100011033.

S.K acknowledges support from National Research Foundation of Korea grant NRF-2019R1A6B2A02100883’

G.A.P.M., V.K., and M.T. were supported by the US Department of Energy, Office of Science, Office of Basic Energy Sciences through the Division of Materials Sciences and Engineering under Contract No. DE-AC02-76SF00515.